Stable, Active, and Methanol-Tolerant PGM-Free Surfaces in an Acidic Medium: Electron Tunneling at Play in Pt/FeNC Hybrid Catalysts for Direct Methanol Fuel Cell Cathodes

Tomasz Kosmala, Nicolas Bibent, Moulay Tahar Sougrati, Goran Dražić, Stefano Agnoli, Frederic Jaouen, Gaetano Granozzi

Stable, Active and Methanol Tolerant PGM-free Surface in Acidic Medium: Electron Tunneling at Play in Pt/FeNC Hybrid Catalysts for Direct Methanol Fuel Cell Cathode

Tomasz Kosmala,[1] Nicolas Bibent,[2] Moulay Tahar Sougrati,[2] Goran Dražić,[3] Stefano Agnoli,[1] Frédéric Jaouen[2*] and Gaetano Granozzi[1]*

1: Department of Chemical Sciences, University of Padua, Via Marzolo 1, 35131 Padova, Italy

2: ICGM, Univ. Montpellier, CNRS, ENSCM, Montpellier, France

3: Department of Materials Chemistry, National Institute of Chemistry, Hajdrihova 19, 1001 Ljubljana, Slovenia

KEYWORDS: hybrid catalyst, core shell, electron tunneling, direct methanol fuel cell, methanol tolerance, model system, ORR, Fe_2O_3

Corresponding Authors

*frederic.jaouen@umontpellier.fr, stefano.agnoli@unipd.it.

ABSTRACT

PGM-free catalysts have high initial activity for O_2 reduction reaction, but suffer from low stability in acid medium in PEMFC and DMFC. Here, we shed light on the atomic-scale structure of hybrid Pt/FeNC catalysts (1-2 wt% of Pt), revealing by STEM and EDXS the presence of Pt@FeO_x particles. The absence of exposed Pt on the surface is confirmed by the suppression of methanol oxidation reaction and CO stripping experiments. The promising application of such Pt/FeNC catalysts, comprising FeN_x sites and Pt@FeO_x particles, is demonstrated at the cathode of DMFC. To gain fundamental understanding on the stability in acid medium and on the intrinsic ORR activity of Pt@FeO_x, we constructed *model* surfaces by depositing FeO_x films with controlled thickness (from 1.0 to 6.4 nm), fully covering the Pt(111) surface, which resulted stable in acid medium in the potential range 0.45 – 1.05 V vs. RHE. The specific ORR activity of Fe_2O_3/Pt(111) increases exponentially with decreasing overlayer thickness, which is explained by the tunneling of Pt electrons through Fe_2O_3. This special phenomenon sheds light onto recently reported excellent durability of Pt/FeNC composites in PEMFC and identify a promising core@shell strategy leading to stable PGM-free surfaces in acid medium, and tolerant to methanol.

INTRODUCTION

The electrochemical oxygen reduction reaction (ORR) to water is a key reaction for electrochemical energy conversion devices such as fuel cells and metal-air batteries.[1–8] A variety of fuel cell (FC) technologies are being developed with operating temperature and chemical environment being defined by the nature of the electrolyte, such as proton exchange membranes (PEM),[9] anion exchange membranes (AEM),[10,11] or solid oxides. Fuel cells based on PEMs (labelled PEMFC when fed with hydrogen, or direct methanol fuel cell, DMFC, when fed with methanol) are more mature than their AEM counterparts and do not suffer from complex issues related to airborne CO_2, a challenge for

alkaline liquid-electrolyte FCs and AEMFCs.[12] PEMFCs in particular are perceived today as the most promising fuel cells for automotive application, while DMFCs can target niche applications where easiness to handle and fuel storage are important.[13–16] The first commercial H_2/air PEMFC cars were deployed in 2017 in Japan and USA and contain Pt-based catalysts both at the anode and cathode, with a higher amount of Pt in the latter.[17] Despite continuous progress in the ORR activity and durability of platinum-based catalysts for acidic medium,[18–21] the high cost and low resources of platinum and any platinum-group-metal remain an issue for reaching the final cost targets of fuel cell stacks and also for sustainability reasons. The mining of new platinum and its recycling significantly contribute to CO_2 emissions in the life-cycle analysis of PEMFC and DMFC devices.[22–24] The impact of platinum-group-metals (PGMs) on the cost and life cycle analysis of DMFCs is stronger than for PEMFCs due to: i) Higher loadings of PGMs at both the anode and cathode of DMFCs compared to PEMFCs; ii) Lower power output per geometric area of membrane electrode assembly of DMFCs *vs*. PEMFCs.

The quest for PGM-free ORR catalysts for PEMFCs and DMFCs has resulted in the demonstration of highly active materials, with FeNC materials comprising atomically dispersed FeN_x sites currently being the most promising subclass of PGM-free catalysts.[25–28]

While progress is observed in the fundamental understanding of the nature of such active sites and the factors that control their initial activity,[29–32] slow progress is currently observed regarding the durability in PEMFC and DMFC of FeNC and other PGM-free materials. All FeNC and other Metal-NC catalysts suffer from rapid activity decrease in operating PEMFCs[2,33,34] and DMFCs.[35–38] The trend is also observed that the higher is their initial ORR activity, the worse is their durability.[2] Recent reports indicate that high initial ORR activity for FeNC materials corroborates with high microporous surface area and also with high Fe leaching rates in oxygenated acidic medium.[39–41] In particular, the simultaneous combination of low electrochemical potential and presence of oxygen seems to trigger Fe demetallation from FeN_x sites, little or not observed in the absence of O_2.[41–43] Such demetallation and degradation is likely related to the *in situ* production of H_2O_2 and reactive oxygen species *via* Fenton

reactions, catalyzed by Fe cations and other 3d transition metal cations.[44,45] Due to similar acidic environment at the cathode of DMFCs and PEMFCs, it is expected that the degradation rates and mechanisms are similar for FeNC catalysts in both devices. This is supported by recent observations of *in situ* formation of iron oxide nanoparticles at the cathode of both PEMFC and DMFC, even for FeNC materials that initially contain only FeN_x sites.[37,41]

Therefore, the identification of rational strategies for improving the durability of PGM-free ORR catalysts in acidic medium is acutely needed. In a recent study, we reported on the stabilization of FeNC by minute amounts of platinum (1-2 wt %).[46] The addition of 1-2 wt % Pt to a given FeNC catalyst resulted in Pt/FeNC composites with similar ORR activity, but with dramatically improved durability in PEMFC. While the ORR activity of FeNC at 0.8 V was divided by *ca* four after PEMFC operation for 50 h at 0.5 V, no measurable change in ORR activity was observed after functionalization of the same FeNC material with 1-2 wt % Pt. A longer durability test in PEMFC for 180 h at 0.5 V confirmed the improved durability. While Pt particles were observed on the SEM images of the Pt/FeNC composites, the lack of increase in activity towards both the ORR and the electroreduction of H_2O_2 for Pt/FeNC relative to FeNC clearly indicated that no metallic Pt was present on the top surface. This was corroborated by the lack of CO-stripping signal of the Pt/FeNC cathode, both before and after the PEMFC durability test at 0.5 V.

In the present work, two Pt/FeNC catalysts were prepared as previously reported,[46] and further investigated with ^{57}Fe Mössbauer spectroscopy at 5 K and scanning transmission electron microscopy (STEM) coupled with energy-dispersive X-ray spectroscopy (EDXS). They were also electrochemically characterized for ORR catalysis with a rotating disk electrode (RDE) in the presence of methanol, as well as at the cathode of DMFC. The STEM-EDXS results show that both large and small Pt particles in these Pt/FeNC hybrid catalysts are covered with a thin shell rich in Fe and O, while ^{57}Fe Mössbauer spectroscopy at 5 K reveals the presence of ferric oxide, which is absent in the reference FeNC material. The electrochemical results identify the complete tolerance to methanol of these Pt/FeNC powder

catalysts. DMFC results with Pt/FeNC cathodes comprising only 40-80 μg_{Pt} cm^{-2} (4 mg total mass of Pt/FeNC per cm^2) showed promising power performance compared to state-of-art Pt/C cathodes with 2000 μg_{Pt} cm^{-2}, advantageously allowing the utilization of high methanol concentration at the anode without any drawback. In order to better understand the stability and possible activity of Pt@FeO_x core-shell particles, electrochemical studies were then performed in acidic electrolyte on *model* surfaces prepared *via* the deposition of ultrathin films of Fe_2O_3 on Pt(111). These studies revealed unexpected stability in acidic medium in the region 0.45 – 1.05 V *vs.* RHE and moderate ORR activity when the Fe oxide layer is ≤ 3.2 nm. The ORR activity of Fe_2O_3 layers on Pt(111) was negatively correlated with layer thickness, which can be explained by electron tunneling effect from the core through the shell. The insights gained from *model* surfaces of Fe_2O_3 layers on Pt(111) and advanced characterization of the present Pt/FeNC hybrid materials explain well the methanol tolerance and lack of CO stripping signal of the latter. Overall, these insights can trigger novel approaches for the design of PGM-free or PGM-based catalysts for ORR and HOR by changing the nature of the metal, either in the core or in the shell, with tuned selectivity and tolerance to a range of fuels and chemicals.

EXPERIMENTAL SECTION

Pt/FeNC powder catalysts synthesis: $Fe_{1.0}$d was synthesized from ZIF-8, a Zn(II) zeolitic imidazolate framework (Basolite Z1200 from BASF), Fe(II) acetate and 1,10-phenanthroline (phen). 800 mg of ZIF-8, 200 mg of phen and 31.5 mg of Fe(II) acetate were poured into a ZrO_2 crucible together with 100 ZrO_2 balls (5 mm diameter), defining a content of 1 wt% Fe in the catalyst precursor. After being sealed in ambient atmosphere, the crucible was subjected to 4 cycles of 30 min ballmilling at 400 rpm (Fritsch Pulverisette 7 premium). The resulting catalyst precursor was flash-pyrolyzed at 1050°C in Ar for 1 h. Then 300 mg of $Fe_{1.0}$d was impregnated with 550 µL (stepwise, 100 µL at a time with grinding for each addition) of an aqueous solution of $Pt(NH_3)_4Cl_2 \cdot H_2O$. The concentration of the Pt salt solution was adjusted in order to reach 1.0 or 2.0 wt % Pt in the hybrid catalysts (9.9 and 17.9 mg/mL for 1 and 2 wt

% Pt, respectively). The impregnated sample was then dried for 2 h in an oven at 80°C under air. The dry powder was loaded in a quartz boat, itself in a quartz tube and ramp-heated under N_2 flow from 300 to 560°C at a rate of 4°C per minute. The gas flow was then switched from N_2 to 5% H_2 in N_2 for 2 h at 560°C. After that, the split hinge oven was opened and the tube removed from it and let to cool down naturally under N_2 flow. The resulting catalysts are labelled $Pt_{1.0}Fe_{1.0}d$ and $Pt_{2.0}Fe_{1.0}d$, for 1 and 2 wt% Pt added onto $Fe_{1.0}d$, respectively.

STEM/EDXS characterization of $Pt_{2.0}Fe_{1.0}d$: Probe Cs-corrected scanning transmission electron microscope Jeol ARM 200 F, equipped with a cold field emission electron source, was used for imaging $Pt_{2.0}Fe_{1.0}d$, and in particular for imaging the Pt nanoparticles. To minimize the beam damage, 80 keV and low beam current were used. High-angle annular dark-field (HAADF) images were obtained using 68-180 mrad collection half-angles at 24 mrad probe convergence semi-angle. Images were filtered with a non-linear filter, which is a combination of low-pass and Wiener filters.

^{57}Fe Mössbauer spectroscopy characterization of $Pt_{2.0}Fe_{1.0}d$: The ^{57}Fe Mössbauer spectrometer (Wissel, Germany) was operated in transmission mode with a ^{57}Co: Rh source. The velocity driver was operated in constant acceleration mode with a triangular velocity waveform. The velocity scale was calibrated with the magnetically split sextet of a high-purity α-Fe foil at room temperature. The spectra were fitted to appropriate combinations of Lorentzian profiles representing quadrupole doublets, sextets by least-squares methods. Isomer shift values are reported relative to α-Fe at room temperature. The powder catalyst was mounted in a 2 cm^2 holder. Mössbauer measurements at 5 K was performed in a helium flow cryostat (SHI-850 Series from Janis, USA).

Electrochemical characterization in RDE of $Pt_{2.0}Fe_{1.0}d$: We used a Pine MSR Electrode Rotator with a RDE/RRDE precision shaft and glassy carbon tip. The ink with 10 mg catalyst, 108.4 µL Nafion solution (5wt %, Sigma Aldrich), 300 µL ethanol and 36.5 µL ultrapure water (> 18 M Ω) was prepared. The ink was ultrasonicated for 30 min. Then, 7 µL was deposited onto a glassy carbon disk with a diameter of 5 mm leading to a total catalyst loading of 0.8 mg cm^{-2}. The electrodes were then immersed into 0.1 M $HClO_4$ in a glass cell with graphite as counter electrode, and a platinum wire in a separate

compartment, saturated with H_2, acting as a reversible hydrogen electrode (RHE). The rotation rate was 1600 rpm. For break-in, at least 5 cyclic voltammogramms (CVs) were applied between 0.0 and 1.0 V_{RHE} at 10 mV s^{-1} in N_2-saturated electrolyte. If the last two scans did not superimpose, more CVs were applied. Subsequently, CVs were recorded at 1 mV s^{-1} in O_2 saturated electrolyte between 0.1 and 1.0 V_{RHE}, a scan rate sufficiently low to neglect capacitive currents.

DMFC experiments: The anode was a gas diffusion electrode already catalyzed with PtRu/C (2000 μg_{PtRu} cm^{-2}, SIGRACET S10BC). The cathode was either a gas diffusion electrode already catalyzed with Pt/C (2000 μg_{Pt} cm^{-2}, SIGRACET S10BC) or a Fe-N-C cathode obtained by depositing 4.0 mg cm^{-2} of Pt/FeNC from an ink on a gas diffusion electrode (SIGRACET S29BC), resulting in 40 and 80 μg_{Pt} cm^{-2} with $Pt_{1.0}Fe_{1.0}$d and $Pt_{2.0}Fe_{1.0}$d, respectively. The ink was prepared by sonicating for 1 hour 103.2 mg of catalyst, 3.364 mL of 5 wt. % Nafion solution (in lower aliphatic alcohols and 15 wt. % water), 1.682 mL 1-propanol, and 1.403 mL deionized water. The catalyst ink was drop cast in 3 aliquots onto the 25 cm^2 gas diffusion layer, giving a total (all elements) loading of 4 mg·cm^{-2}, then dried at 70 °C for 1 hour. The cathode was hot-pressed onto Nafion 117 with the commercial anode using a pressure of 2 tons and 135 °C for 2 minutes. The cell assembly consisted of a Fuel Cell Technologies Inc. single cell with serpentine flow fields in graphite end plates. The methanol flow rate was 50 mL min^{-1}. The cell temperature, cathode flow rate and absolute pressure were i) 80°C, 1 bar, 400 mL min^{-1} or ii) 90°C, 1.5 bar, 600 mL min^{-1} or iii) 100°C, 2 bars, 600 mL min^{-1}. Polarisation curves were recorded point by point under galvanostatic control, from low to high current densities and then vice versa. For each current density, the cell voltage obtained when increasing the current and then decreasing it was averaged. This average is used to report the polarisation curves.

Preparation of α-Fe_2O_3/Pt(111) surfaces: The α-Fe_2O_3 on Pt(111) surface was prepared by adopting the procedures described in Refs. [47,48]. The surface of the Pt(111) single crystal (MaTeck) was cleaned by cycles of sputtering (1.5 keV, 10^{-6} mbar of Ar, room temperature) and annealing at 1000 K. The residual carbon was removed by annealing in $2.0 \cdot 10^{-7}$ mbar of oxygen at 900 K and, subsequently, the adsorbed oxygen was removed by flash annealing at 1000 K. This procedure was repeated until the

LEED pattern of a clean Pt(111) surface with sharp spots and low background was obtained. The Fe oxide films were grown by repeated cycles of reactive evaporation of Fe onto the clean Pt(111) substrate at $2 \cdot 10^{-5}$ mbar O_2 partial pressure and keeping the substrate at 800 K. Then, the sample was annealed at 1050 K at $4 \cdot 10^{-3}$ mbar O_2 to fully convert the Fe oxide phases to α-Fe_2O_3. Oxygen was introduced in the preparation chamber by means of a capillary located at only *ca* 1 cm from the sample.

Structural characterization of α-Fe_2O_3/Pt(111) surfaces: The composition of the samples and the chemical changes induced by the exposure to the EC environment were investigated by XPS using an EA 125 Omicron electron analyzer equipped with five channeltrons, working at a base pressure of $2 \cdot 10^{-10}$ mbar. The XPS data were collected at RT with the Mg Kα line (hν = 1253.6 eV) of a non-monochromatic dual-anode DAR400 X-ray source using 0.1 eV energy step, 0.5 s collection time and 20 eV pass energy. The binding energy (BE) scale was calibrated using a gold sample (Au 4f at 84 eV). The film thickness was determined before and after the electrochemical treatments by angle-resolved XPS (AR-XPS) measurements using the Fe_{2p} and Pt_{4f} photoemission peak intensity, according to the method reported in Ref. [49]. Low energy electron diffraction (LEED) patterns were acquired using an incident electron beam with energy between 30 and 80 eV. All LEED patterns were recorded at room temperature.

Electrochemical studies on α-Fe_2O_3/Pt(111) surfaces: Cyclic voltammetry (CV) and methanol tolerance of α-Fe_2O_3/Pt(111) UT films were investigated in a conventional *ex situ* three-electrode cell. A glassy carbon rod was used as counter electrode and a saturated calomel electrode (SCE) as reference electrode. All potentials reported are however referred to the reversible hydrogen electrode (RHE) scale, and the conversion was done according to the equation: E(RHE) = E(SCE) + 0.258 + 0.059 × pH. A custom-designed sample holder with an area of 0.502 cm^2 was used.

In Situ Electrochemical Scanning Tunneling Microscopy (EC-STM) studies on α-Fe_2O_3/Pt(111) surfaces: The *in situ* EC-STM measurements were carried out using a home-built EC-STM at constant current mode, as described by Wilms et al.[50]. The tunneling tips were electrochemically etched from a 0.25 mm tungsten wire in 2 M KOH solution and, subsequently, cleaned in high purity water, dried and

coated by passing the tip through a drop of hot glue. Platinum wires were used as counter and reference electrodes. The Pt reference electrode was calibrated vs. SCE in Ar-saturated 0.1 M $HClO_4$. The image analysis was carried out using the software WSxM 5.0.

RESULTS AND DISCUSSION

Two hybrid catalysts labelled $Pt_{1.0}Fe_{1.0}$d and $Pt_{2.0}Fe_{1.0}$d were synthesized as previously reported.[46] The synthesis involves first the preparation of an Fe-N-C catalyst, $Fe_{1.0}$d, with 1.0 standing for 1 wt% Fe before pyrolysis and d for dry ball milling. $Fe_{1.0}$d was then impregnated by given amounts of a Pt salt to result in 1.0 or 2.0 wt % Pt in the hybrid catalyst, then dried and annealed at 560°C in 5% H_2 in N_2 (see Methods). While $Pt_{1.0}Fe_{1.0}$d and $Pt_{2.0}Fe_{1.0}$d were demonstrated to be free of metallic platinum on their surface and they achieved at best only 1/50th the ORR-activity of Pt/C,[46] the yet unknown structure and reactivity of Pt in such materials precludes any a priori statement on their tolerance to methanol while catalyzing the ORR. **Figure 1a** shows no significant difference in the ORR polarisation curves measured for $Pt_{1.0}Fe_{1.0}$d in acid in the absence of methanol and after addition of 0.1 or 2.0 M methanol. This clearly indicates that both Pt in $Pt_{1.0}Fe_{1.0}$d and the Fe-based actives sites in $Pt_{1.0}Fe_{1.0}$d are inactive towards methanol oxidation up to 1.0 V *vs.* a reversible hydrogen electrode (RHE). For Fe-based active sites, this comes to no surprise since all other FeNC catalysts previously studied to that end showed complete methanol tolerance.[51,52] In contrast, the methanol tolerance of Pt here is different from the well-known methanol electro-oxidation activity of state-of-art Pt/C, when metallic Pt is exposed to the surface.[53,54] The present hybrid Pt/FeNC catalysts are therefore promising for application at the cathode of DMFC, being tolerant to methanol crossover from the anode to the cathode and much more durable than FeNC alone, as previously shown in PEMFC.[46] $Pt_{1.0}Fe_{1.0}$d and $Pt_{2.0}Fe_{1.0}$d were therefore evaluated at the cathode of DMFC.

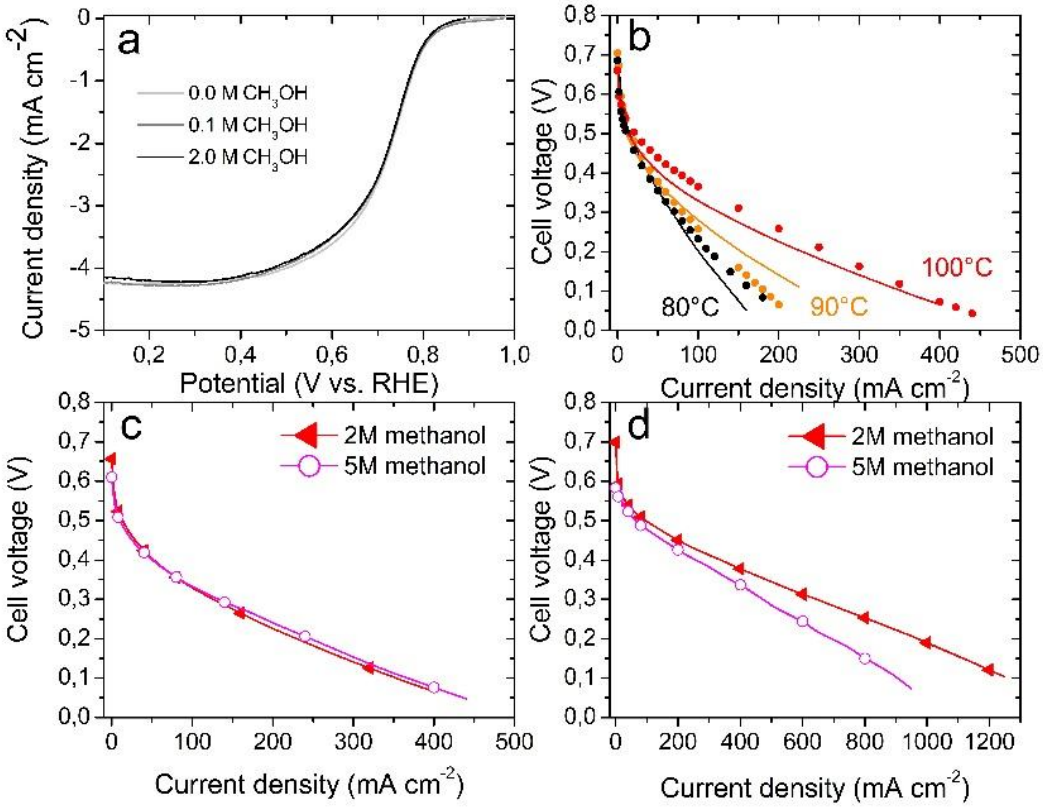

Figure 1. Electrochemical characterisation of hybrid Pt/FeNC catalysts and comparison to a commercial Pt/C cathode. a) Effect of methanol concentration in 0.1 M $HClO_4$ on ORR polarisation curves measured in RDE for $Pt_{1.0}Fe_{1.0}d$ at a loading of 0.8 mg cm^{-2} (8 $\mu g_{Pt} \cdot cm^{-2}$). b) DMFC polarisation curves at 80, 90 or 100°C with cathodes based on $Pt_{1.0}Fe_{1.0}d$ (circles) or $Pt_{2.0}Fe_{1.0}d$ (solid curves) at a total cathode catalyst loading of 4 $mg \cdot cm^{-2}$ (40 and 80 μg_{Pt} cm^{-2} with $Pt_{1.0}Fe_{1.0}d$ and $Pt_{2.0}Fe_{1.0}d$, respectively). c) Effect of methanol concentration on the DMFC polarisation curves at 100°C with a $Pt_{2.0}Fe_{1.0}d$ cathode at a total cathode catalyst loading of 4 $mg \cdot cm^{-2}$ (80 μg_{Pt} cm^{-2}. d) Effect of methanol concentration on the DMFC polarisation curves at 100°C with a commercial Pt/C cathode (2000 $\mu g_{Pt} \cdot cm^{-2}$). For a), the rotation rate was 1600 rpm. For all DMFC measurements, the anode was PtRu/C (2 $mg_{PtRu} \cdot cm^{-2}$), the membrane was Nafion 117. For b), the cell temperature was 80, 90 or 100°C and the methanol concentration was 2.0 M. For c) and d), the methanol concentration was 2.0 or 5.0 M and the cell temperature was 100°C.

The effect of cell temperature was first investigated, highlighting strong improvement from 80 to 100°C (**Figure 1b**). The cell performance obtained with $Pt_{1.0}Fe_{1.0}d$ and $Pt_{2.0}Fe_{1.0}d$ is comparable, the difference lying within the reproducibility error. In particular, the cell performance at high voltage (kinetically controlled region) is very similar for both cathode catalysts, as expected from our previous work.[46] Since the content of 1 wt % Pt was shown in PEMFC to be the lower-end limit for complete durability over at least 50 h in PEMFC,[46] we then focused the DMFC measurements on the $Pt_{2.0}Fe_{1.0}d$ cathode. The latter showed complete durability for all the 50 h PEMFC tests performed at our laboratory and for different batches of $Pt_{2.0}Fe_{1.0}d$. The effect of methanol concentration at the anode feed was then investigated, and the results confirm the methanol tolerance observed in RDE, with unnoticeable change from 2 to 5 M feed (**Figure 1c**). For comparison, the same measurements were performed with a commercial Pt/C cathode with high Pt loading, and the results show an important decrease of cell performance from 2 to 5 M methanol feed (**Figure 1d**). The effect would be even more significant for lower Pt loadings in Pt/C cathodes, due to enhanced CO poisoning on regular Pt particles with surface-exposed Pt. This *operando* poisoning limits the methanol concentration that can be used in DMFC systems, with a strong impact on the footprint of the methanol reservoir and implies high cathode Pt loadings. The $Pt_{2.0}Fe_{1.0}d$ cathode is therefore promising to overcome those limitations. The current density at 0.3 V and 100°C with 5 M methanol feed is about 110 mA cm^{-2} with the $Pt_{2.0}Fe_{1.0}d$ cathode (80 μg_{Pt} cm^{-2}), *ca* 25 % of the current density reached in the same conditions with the commercial Pt/C cathode (2000 μg_{Pt} cm^{-2}) (**Figure 1c-d**, magenta curves). While the absolute performance is presently lower, due to lower ORR kinetics, a high margin exists to approach the same performance. This might be achieved for example by increasing the Pt content on FeNC, if such Pt structures have moderate ORR activity. Alternatively, it might be achieved by increasing the ORR activity of the FeNC substrate. In the former approach, the increased content of Pt should however be carried out by design, leading to the synthesis of methanol-tolerant Pt structures.

The structure of $Pt_{2.0}Fe_{1.0}d$ was then investigated with STEM-EDXS in order to better understand the structure of the Pt particles and why they are inactive toward methanol oxidation. In our original paper

on hybrid Pt/FeNC catalysts,[46] the distribution of Pt particles on the Fe- and N-doped carbon support of $Pt_{1.0}Fe_{1.0}d$ was revealed by STEM (Figure 2 and Figure S1 in Ref. [46]). Elemental mapping with EDXS on a catalyst area comprising both the FeNC background and particles expected to be Pt-rich confirmed the strong presence of Pt, but no information on the element distribution inside the particle could be obtained due to limits intrinsic to the microscope (Figure S1 in Ref. [46]). Here, a STEM image of a large area of $Pt_{2.0}Fe_{1.0}d$ shows again large and small bright particles (**Figure S1a**). These particles are identified by EDXS to be Pt-rich (**Figure S1b**). EDXS mapping on Fe identifies both a diffuse background signal related to Fe that is atomically dispersed in the support ($Fe_{1.0}d$) but also a localized Fe signal matching with the position of the Pt-rich particles (**Figure S1b-c**). While this could be interpreted as the presence of PtFe alloy particles, EDXS mapping on oxygen reveals an even better match between Fe and O than between Fe and Pt (**Figure S1c-d**), suggesting that Fe and O are intimately organized. The overlay between the Pt and Fe signals further suggests $Pt@FeO_x$ core-shell structures (**Figure S1e**). Higher resolution STEM and EDXS mapping on a single Pt particle further support this view (**Figure 2**). The high-angle annular dark-field (HAADF), bright field STEM images (**Figure 2a-b**), EDXS mapping on Pt, Fe, O and the overlay of the signals for Pt and Fe (**Figure 2c**) identify a Pt core of *ca* 7.5 nm and a Fe-oxide shell of *ca* 1.2-1.3 nm. The elemental profile lines in **Figure 2d** further identify the Fe and O shell, extending beyond the Pt core. This $Pt@FeO_x$ structure was observed on large and small particles. **Figure S2** shows another Pt particle with a different shape and size than that in **Figure 2,** but having a similar thickness of the FeO_x shell, *ca* 1.3 nm.

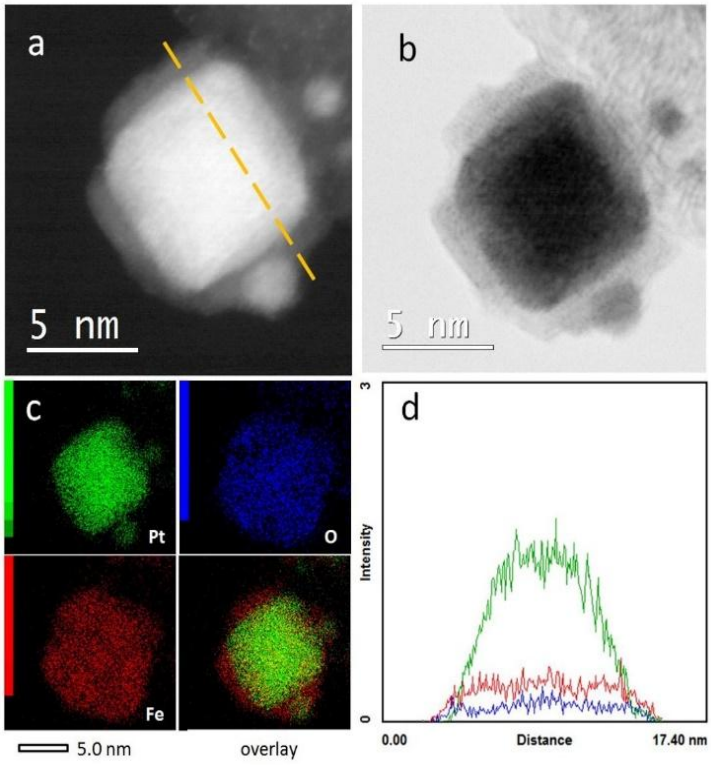

Figure 2. STEM-EDXS characterization of a single Pt-rich particle in $Pt_{2.0}Fe_{1.0}$d. a) HAADF and b) bright field images, c) EDXS elemental mapping for Pt (green), iron (red), oxygen (blue) and overlay Pt and Fe (lower left hand side corner), d) intensity profiles of the various elements along the line indicated in a).

$Pt_{2.0}Fe_{1.0}$d was then characterized with ^{57}Fe Mössbauer spectroscopy at 5 K. The importance of performing ^{57}Fe Mössbauer spectroscopy at low temperature for characterizing FeNC materials was recently put forth in several reports.[31,32] Measurements above *ca* 60 K lead to an ambiguous quadrupole doublet signal with low quadrupole splitting value (*ca* 1 mm s^{-1}), that may be assigned either to specific FeN_4 sites or to nanometric Fe oxide particles. At 5 K, the latter usually become paramagnetic, leading to a sextet spectral component while FeN_4 sites still result in a doublet component.[55] The spectrum of $Pt_{2.0}Fe_{1.0}$d (**Figure S3** and **Table S1**) comprises a number of components that had previously been observed by us in the room-temperature spectrum of H_2-$Fe_{1.0}$d (Figure 3b in Ref [46]). The latter is the reference material, obtained after subjecting $Fe_{1.0}$d to the same annealing treatment in 5%H_2/N_2 at 560°C as applied to prepare Pt/FeNC hybrids from $Fe_{1.0}$d in the present work. The ^{57}Fe Mössbauer

spectrum of $Pt_{2.0}Fe_{1.0}d$ comprises two quadrupole doublets D1, D2 assigned to atomically dispersed FeN_4 moieties of different spin and oxidation states (from DFT-calculated quadrupole splitting values and experimental spectroscopic characterisations of a model Fe-N-C catalyst, D1 was identified to be mainly a $Fe(III)N_4C_{12}$ single-metal-atom site in high-spin state and D2 a $Fe(II)N_4C_{10}$ single-metal-atom site in low- or medium-spin state),[31] a singlet assigned to γ-Fe and a sextet assigned to α-Fe. However, one additional sextet component (accounting for 16% of the signal, **Table S1**) is observed in the ^{57}Fe Mössbauer spectrum of $Pt_{2.0}Fe_{1.0}d$ at 5 K that is absent in the room-temperature spectrum of H_2-$Fe_{1.0}d$, and unambiguously assigned to high-spin ferric oxide, most probably Fe_2O_3. This component fits well with the observation by STEM-EDXS of a nanometric Fe-oxide shell around Pt nanoparticles in $Pt_{2.0}Fe_{1.0}d$.

These high resolution STEM-EDXS and low-temperature ^{57}Fe Mössbauer spectroscopy characterizations of $Pt_{2.0}Fe_{1.0}d$ therefore suggest that a fraction of Fe from H_2-$Fe_{1.0}d$ migrated on the surface during the reductive annealing of the Pt salt impregnated on H_2-$Fe_{1.0}d$, leading to the $Pt@FeO_x$ structures supported on the Fe- and N-doped carbon substrate. These novel insights explain i) why the addition of 1-2 wt% Pt to H_2-$Fe_{1.0}d$ followed by the present annealing treatment did not lead to significant increase in the initial ORR activity relative to H_2-$Fe_{1.0}d$, and ii) why no CO stripping signal was observed for $Pt_{1.0}Fe_{1.0}d$.[46] While the addition of 1-2 wt % Pt to H_2-$Fe_{1.0}d$ did not lead to an ORR-activity increase, it resulted in a spectacular stabilization during operation in PEMFC with almost no performance loss at 0.5 V and almost no activity increase or decrease at 0.8 V, even after 180 h operation (Figure 10 in Ref. [46]). This must imply that the Pt particles remained covered by the iron oxide shell *in operando*, in spite of the expected leaching of ferric oxide as ferrous cations at *e.g.* 0.5 V in the acidic medium of PEMFCs. We assign the stability of ferric oxide on metallic Pt nanoparticles to a strong interaction between ferric oxide and Pt, leading to a stabilization of the non-PGM overlayer. It is of interest to note that $Pt@Fe_2O_3$ nanoparticles are well known in the field of materials science, with potential applications in magnetic storage, catalysis and biological labelling.[56–59] These novel structural insights into the nature of Pt in $Pt_{1.0}Fe_{1.0}d$ and $Pt_{2.0}Fe_{1.0}d$ also raise new questions on the true reason for

the observed durability of these hybrid catalysts in PEMFC. Do Pt@Fe_2O_3 nanoparticles act as scavengers for peroxide or reactive oxygen species, protecting the FeN_x active sites from deactivation or degradation? Or do they have intrinsic ORR activity that is comparable to that of FeN_x active sites, leading to apparent similar ORR activities for $Fe_{1.0}$d, H_2-$Fe_{1.0}$d, $Pt_{1.0}Fe_{1.0}$d and $Pt_{2.0}Fe_{1.0}$d? To disentangle these different possibilities, we performed studies on *model* flat surfaces of Fe_2O_3 layers of controlled thickness grown on Pt(111).

Fe_2O_3/Pt(111) *model* surfaces were prepared according to a modified version of the procedure described by Freund's group.[48,60] Briefly, iron atoms were evaporated at constant rate on the clean Pt(111) surface in an atmosphere of $2 \cdot 10^{-5}$ mbar O_2 at 800 K. To improve the crystalline order and guarantee complete oxidation, a post annealing at 1050 K in $4 \cdot 10^{-3}$ mbar O_2 for 45 minutes was necessary. The atomic structure and chemical composition of the resulting Fe_2O_3 ultrathin films were investigated by low energy electron diffraction (LEED) and X-ray photoemission spectroscopy (XPS). **Figure S4** reports the LEED patterns of the clean Pt(111) substrate and of Fe_2O_3/Pt(111) ultrathin film with an average thickness of 3.2 nm, as determined by angle-resolved(AR)-XPS measurements. The diffraction pattern corresponds to a α-Fe_2O_3(0001)-(1 x 1) surface with a hexagonal unit cell with a lattice constant of 5.0 Å that is rotated by 30° with respect to the unit cell of the Pt(111) surface.[47]

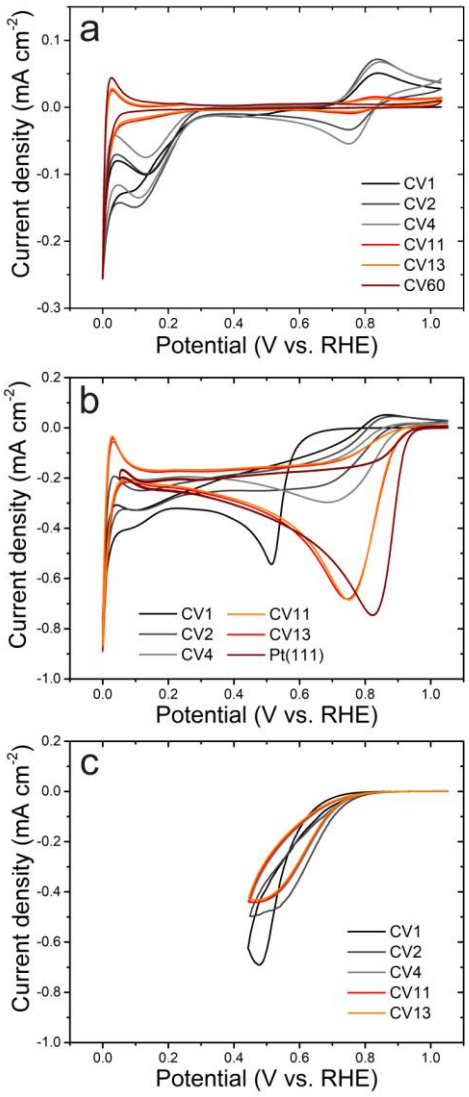

Figure 3. Cyclic voltammograms of the 3.2-Fe_2O_3/Pt(111) film in (a) Ar-saturated and (b-c) O_2-saturated 0.1 M $HClO_4$ solution at a scan rate of 20 $mV \cdot s^{-1}$ between (a-b) 1.05 and 0.0 V *vs*. RHE and (c) 1.05 and 0.45 V *vs*. RHE.

The stoichiometry of the Fe_2O_3 ultrathin film is confirmed by the Fe_{2p} core-level XPS data reported in **Figure S5a**. A clear satellite is observed at a binding energy of 719.3 eV, which is associated with Fe^{3+} species[61]. Moreover, the O_{1s} photoemission line (**Figure S5b**) exhibits only one component at 529.5 eV, indicating a pure hematite phase[61]. Lastly, the Fe/O atomic ratio determined by XPS was 2/3, as expected for pure Fe_2O_3. To confirm the full coverage of the Pt(111) surface by the iron oxide layer, the C_{1s} energy region was checked after dosing hundreds of Langmuir of CO at room temperature. The lack of any C_{1s} signal confirmed the absence of adsorbed CO, implying the absence of surface-exposed Pt

sites. By adopting the same synthesis protocol, but reducing the amount of the evaporated Fe, it was possible to grow Fe_2O_3 with thickness of 1.0, 1.6 nm and 6.4 nm, with analogous structural and morphological properties. This gives us therefore four model surfaces with thickness of 1.0, 1.6, 3.2 and 6.4 nm of Fe_2O_3 on Pt(111), labelled as x-Fe_2O_3/Pt(111) where x is the thickness in nm. For the thinnest film of 1 nm, we verified again with XPS of C_{1s}, after dosing hundreds of Langmuir of CO at room temperature, that no CO adsorbed on the 1.0-Fe_2O_3/Pt(111) film, verifying the absence of surface-exposed Pt (**Figure S6**).

The electrochemical stability of the 3.2-Fe_2O_3/Pt(111) film was evaluated *ex situ* by cyclic voltammetry (CV) in Ar- or O_2-saturated 0.1 M $HClO_4$ solution using a standard three-electrode cell. **Figure 3a** shows the CVs measured in Ar-saturated electrolyte between 1.05 V and 0.0 V *vs.* RHE. The negative- and positive-going scans of the second CV (CV2) show two redox peaks at 0.75 V and 0.83 V *vs.* RHE, respectively. Those peaks are absent from the CV of the clean Pt(111) surface (not shown) and can therefore be associated with the Fe^{3+}/Fe^{2+} redox couple. Their intensity is decreasing with the number of cycles (CV4 to CV60), suggesting the progressive dissolution of the α-Fe_2O_3 film. This interpretation is supported by XPS measurements showing a constant decrease of the ratio Fe_{2p}/Pt_{4f} from the photoemission peaks (not shown). Interestingly, the redox couple is not observed when the 3.2-Fe_2O_3/Pt(111) surface is cycled between 0.55 and 1.05 V *vs*. RHE (see **Figure S7**). The appearance of the redox couple centered at 0.79 V *vs.* RHE seems therefore conditioned by the previous occurrence of the reduction event related with the reduction peak observed at *ca*. 0.12 V *vs.* RHE in the negative-going scans (CV1-4 in **Figure 3a**). This is especially obvious for CV1, where no reduction peak is observed at 0.75 V vs. RHE in the first negative-going scan while the oxidation peak at 0.83 V is clearly visible in the subsequent positive-going scan. This might imply that the Fe^{3+}/Fe^{2+} redox couple is not intrinsic to α-Fe_2O_3 phase itself, but stems from a reduced Fe oxide top-surface layer formed on the surface of α-Fe_2O_3 while the potential applied is in the range of 0.12-0.0 V *vs*. RHE.

A very similar behavior is observed when the acid medium is saturated with oxygen. When scanning the potential in the window 1.05 – 0.0 V *vs*. RHE (**Figure 3b**), the iron oxide layer is progressively dissolved as deduced from the shift of the onset potential of the ORR toward more positive values, characteristic for a bare Pt(111) surface. Analogous conclusion of identical dissolution behavior in Ar- and O_2-saturated acid electrolytes can also be deduced from the analysis of the Fe_{3p}/Pt_{4f} photoemission signal, which eventually strongly decreases after several cycles in the 0.0-1.05 V potential window, regardless of the Ar- or O_2-saturation (**Figure S8a**).

In order to avoid dissolution of Fe_2O_3 in the subsequent experiments, the lower-limit potential during the scans was set to 0.45 V *vs*. RHE, well above the onset of the reduction peak of the Fe_2O_3 film located at *ca* 0.3 V *vs*. RHE. The CVs were recorded until a stable response was observed, then the sample was analyzed by XPS to determine possible chemical transformations as well as to measure the Fe-oxide film thickness. No chemical changes were induced in those cycling conditions (13 cycles between 1.05 and 0.45 V vs. RHE in O_2-saturated 0.1 M $HClO_4$, **Figure S8b**, curve 4) and the thickness of the iron oxide film after the cycling was estimated to be 92 ± 4% of the initial value. These results indicate that the Pt substrate stabilizes the α-Fe_2O_3 thin film in acidic medium in the potential region 0.45 – 1.05 V *vs*. RHE.

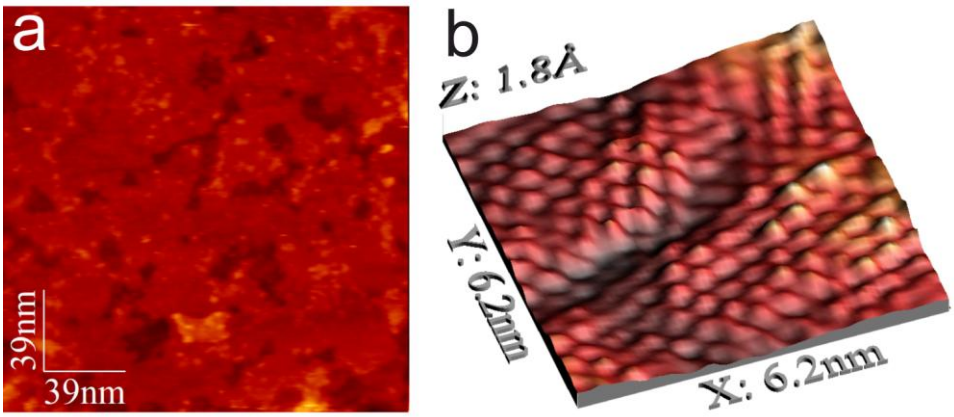

Figure 4. Low- (a) and high-resolution EC-STM images (b) of 1.6-Fe_2O_3/Pt(111) in Ar-saturated 0.1 M $HClO_4$ solution at 1.05 V *vs.* RHE. Tunneling parameters: U_b = -900 mV, I_t = 4.8 nA (a) and U_b = -697 mV, I_t = 4.8 nA (b).

In order to get an insight at the atomic level into the morphology and stability of the Fe_2O_3/Pt(111) system, the film with a nominal thickness of 1.6 nm was investigated by *in situ* electrochemical scanning tunneling microscopy (EC-STM). This technique directly demonstrates the stability of the Fe_2O_3/Pt(111) system even at the atomic level. **Figure 4** shows low- and high-resolution STM images acquired in Ar-saturated 0.1 M $HClO_4$ solution at 1.05 V *vs.* RHE. The Fe_2O_3 layer fully covers the Pt(111) surface, forming flat terraces characterized by an average surface roughness (R_a) and root mean square (RMS) roughness (see supporting information for details) for of ~ 0.9 and ~ 1.3 Å, respectively, where a primitive hexagonal unit cell, with the lattice parameter of ~ 5 Å can be clearly identified **(Figure 4b**).

Figure S9 reports a series of potentiodynamic EC-STM images starting from 1.05 V down to 0.45 V *vs.* RHE. The red arrow on all panels indicates the same position on the surface. The electrode potential was scanned in the cathodic direction without observing any significant change on the surface (**Figure S9b-c**). Then, the potential was scanned back up to 1.05 V *vs.* RHE (**Figure S9d-f**). No changes in the morphology were observed in this potential window (0.45–1.05 V *vs.* RHE). Moreover, no differences were observed after 24 h in 0.1 M $HClO_4$ at 0.6 V *vs.* RHE and 100 cycles between 1.05 V and 0.45 V *vs.* RHE (**Figure S10a**) which is confirmed by the R_a and RMS roughness analysis (**Table S2**). No Pt features were observed also in the CV in the region of 0.45 to 1.05 V vs. RHE, after the same protocol (**Figure S10b**), indicating that no Pt surface was exposed even after potential hold and potential cycling in this potential range. Overall, the experimental data suggest that in the potential window 0.45 – 1.05 V *vs*. RHE, the ultrathin hematite film is highly stable in acid conditions. The origin of this high stability is not clear yet, and several phenomena could be involved. Recent DFT calculations ascribed the increased

stability in alkaline conditions of NiO_x ultrathin films on Pt(111) surface with respect to the bulk counterpart to the strong adhesion energy with the underlying metal[62]. From calculated Pourbaix diagrams, a monolayer of NiOOH on Pt(111) was predicted to be stable down to a potential of *ca* 0.65 V vs. RHE while the bulk NiOOH phase was unstable already below 1.4 V vs. RHE.[62] Similar strong stabilization was also calculated for Mn- and Co-oxy(hydroxides) on Pt(111) vs. the bulk oxy(hydroxides).[62] The magnitude of stabilization predicted for these metal-oxy(hydroxides) films on Pt(111) are compatible with the stability down to 0.45 V vs. RHE for Fe_2O_3 thin film on Pt(111) observed in this work. In addition, the peculiar electronic properties of ultrathin films and changes in the electronic structure at the interface between Fe_2O_3 and Pt(111) can play a role. In particular, the Pt 5d band strongly hybridizes with Fe 3d and O 2p states at the interface and even in the inner layers[63,64], which can influence the stability of the films.

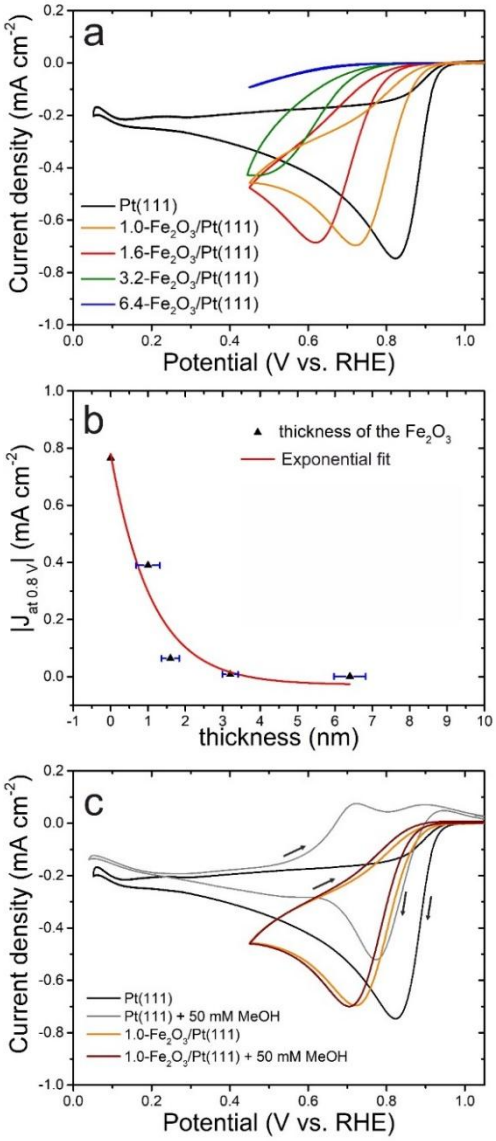

Figure 5. a) Comparison of CVs for the different thickness of Fe_2O_3/Pt(111) in O_2-saturated 0.1 M $HClO_4$ electrolyte; b) Absolute value of ORR current density at 0.8 V *vs.* RHE measured with CV in O_2-saturated 0.1 M $HClO_4$ as a function of the thickness of the Fe_2O_3 thin-film layer on Pt(111). The red curve shows the fitting of the experimental data with an exponentially decreasing law (see **Table S4**); c) Effect of addition of 50 mM methanol to the CVs of 1.0-Fe_2O_3/Pt(111) and Pt(111) in O_2-saturated 0.1 M $HClO_4$ solution. The scan rate was 20 mV s^{-1} for all measurements.

Let us know examine the ORR activity of the different Fe_2O_3/Pt(111) films. When examining the 3.2-Fe_2O_3/Pt(111) film that has been discussed hitherto, we find a poor ORR activity in comparison to the

clean Pt(111) surface, with *ca* 300 mV negative shift (compare the green and black curves in **Figure 5a**). On the other hand, the STEM analysis of the core@shell particles in $Pt_{2.0}Fe_{1.0}d$ revealed a thickness of the Fe_2O_3 shell below 1.5 nm. Therefore, the effect of the iron oxide film thickness on the ORR activity was further investigated on the 1.0-, 1.6- and 6.4-Fe_2O_3/Pt(111) films. As observed in **Figure 5a**, there is an inverse correlation between ORR activity and the Fe_2O_3 film thickness for the Fe_2O_3/Pt(111) ultrathin films. At the lowest thickness (1.0 nm), the kinetically controlled region of the polarisation curve of 1.0-Fe_2O_3/Pt(111) is *ca* only 80 mV negative compared to that of clean Pt(111). In terms of ORR activity at 0.9 V *vs*. RHE, the 1.6 and 1.0 nm Fe-oxide layers on Pt(111) reach *ca* $1/70^{th}$ and $1/8^{th}$ the ORR activity of Pt(111), respectively. This is because although the metal surface is fully covered by α-Fe_2O_3, even for the 1.0 nm thick film, the electrons from the Pt metallic substrate can tunnel through the oxide layer and catalyze the oxygen reduction on the electrode surface[65–67]. As the oxide thickness increases, tunneling is progressively suppressed and the top surface then shows catalytic properties similar to the bulk phase of the overlayer, with little to no ORR activity expected for bulk Fe_2O_3 in acidic medium. **Figure 5b** and **S11** better show the correlation between Fe_2O_3 layer thickness and ORR activity at 0.8 and 0.9 V *vs*. RHE, respectively. The lower potential of 0.8 V allows a more accurate reading of ORR activity for thick Fe_2O_3 overlayer, while 0.9 V is more convenient to compare to the ORR activity measured for a bare Pt(111) surface. In both cases, the experimental data of ORR activity vs. Fe_2O_3 thickness could be fitted with an exponentially-decaying law, supporting the electron tunneling hypothesis.

These results suggest that the observed ORR activity in the Pt/FeNC powder catalysts may arise in part from Pt@FeO_x nanostructures and not only from FeN_x centers. To estimate the activity that may be expected from Pt@Fe_2O_3 nanostructures in the $Pt_{2.0}Fe_{1.0}d$ powder (J_{Fe2O3}), one needs to estimate the surface specific activity of Fe_2O_3 (i_s) and the surface area of Fe_2O_3 in the Pt/FeNC layer per geometric area of glassy carbon (S). The value of i_s may be estimated from the Faradaic current density observed at 0.8 V *vs*. RHE in **Figure 5a**, red curve (0.065 $mA \cdot cm^{-2}$), corresponding to the 1.6 nm thick film. The latter is close to the Fe-oxide thicknesses observed in $Pt_{2.0}Fe_{1.0}d$. Then, the surface area of Fe_2O_3 in the

RDE active layer can be estimated assuming that the Pt cores have a single diameter, r (assumed between 2.5 and 4.0 nm), and the Fe-oxide shells have a fixed thickness of 1.6 nm (see supporting text). The calculations lead to S-values between *ca* 11 and 24 cm^2 Fe_2O_3 per cm^2 geometric area for r = 4 and 2.5 nm, respectively. The former radius seems to better represent $Pt_{2.0}Fe_{1.0}d$, leading to *ca* 0.6 wt % Fe being present as Fe_2O_3 (*ca* 20 % relative to all Fe), in line with the ^{57}Fe Mössbauer spectroscopy analysis (**Table S1**, 16% Fe as Fe-oxide). The Pt core radius of 4 nm is also in line with the most frequent particle size of *ca* 8 nm reported by us previously for these Pt/FeNC materials (Figure 2 of Ref. [46]). The expected contribution to the ORR activity at 0.8 V *vs.* RHE is then 0.71 $mA \cdot cm^{-2}$ (**Table S3**). This is significantly lower than the total ORR activity of $Pt_{2.0}Fe_{1.0}d$ in 0.1 M $HClO_4$ at 0.8 V *vs*. RHE (*ca* 6.8 mA cm^{-2}, Figure 6a in Ref. [46]), and seems to support the stabilisation of FeN_x ORR active sites by less ORR-active Pt@Fe_2O_3 particles. The calculation is however highly sensitive to the assumed i_s value, and the conclusion would be changed assuming the i_s-value measured for 1 nm Fe_2O_3 thickness (0.4 $mA \cdot cm^{-2}$). Future work with better-defined materials, in particular with more uniform Pt particle size in such Pt/FeNC composites, will thus be necessary to strengthen this conclusion, since the calculations also show that the assumed Pt core radius strongly affects the ORR activity contribution from Pt@Fe_2O_3 particles for a fixed Pt content of 2 wt% (**Table S3**).

Finally, the methanol tolerance of the 1.0-Fe_2O_3/Pt(111) film was investigated using our *model* systems. CVs were recorded for Pt(111) and 1.0-Fe_2O_3/Pt(111) in O_2-saturated 0.1 M $HClO_4$ electrolyte (**Figure 5c**) before and after adding the amount of methanol necessary to reach a concentration of 50 mM. Due to the absence of convection of the electrolyte and semi-infinite diffusion mechanisms, the negative-going scans identify best the ORR activity (low methanol concentration at the electrode surface, if the surface is methanol-active) while the subsequent positive-going scans identify best the tolerance to methanol (O_2 concentration at the electrode surface decreased during the negative going scan via ORR, while the methanol concentration was replenished at low potentials). The positive-going scan of the 1.0-Fe_2O_3/Pt(111) surface in 50 mM methanol in O_2-saturated 0.1 M $HClO_4$ shows no features of methanol oxidation indicating complete tolerance to methanol (*i.e.* no activity for methanol oxidation reaction).

This is also supported by the nearly superimposed negative-going scans in O_2-saturated 0.1 M $HClO_4$, with or without 50 mM methanol (orange and red curves in **Figure 5c**). Such a result is in line with the lack of methanol oxidation activity seen for $Pt_{1.0}Fe_{1.0}d$ (**Figure 1a**). In contrast, the positive-going scan of Pt(111) in 50 mM methanol in O_2-saturated 0.1 M $HClO_4$ shows methanol oxidation onset at *ca* 0.5 V vs. RHE and the sign of the current density even becomes positive *ca* 0.7 V vs. RHE indicating that the methanol oxidation current is larger than the oxygen reduction current. The methanol activity of Pt(111) is also seen in the difference between the negative-going scans in O_2-saturated 0.1 M $HClO_4$, with or without 50 mM methanol (black and grey curves in **Figure 5c**). In summary, the 1.0-Fe_2O_3/Pt(111) surface is methanol tolerant, revealing that the 1 nm thick oxide surface on top pf Pt(111) imparts methanol tolerance, while reducing the ORR activity relative to a bare Pt(111) surface. A similar enhancement of the poisoning tolerance imparted by ultrathin films has previously been observed for the Co_3O_4/CoO/Pd(1oo) system for ORR in alkaline conditions[65].

We note that the overall structural and electrochemical characterization results of the present study bear a strong analogy with a recent report from Gasteiger's group on a powder catalyst consisting of Pt nanoparticles deposited on TiO_x, themselves supported on carbon black and finally subjected to a thermal treatment at 400°C in 5% H_2/Ar (labelled $Pt/TiO_x/C^{400°C,\ H2}$ in Ref. [68]). The ORR activity normalized by the Pt mass was 50 times lower for $Pt/TiO_x/C^{400°C,\ H2}$ compared to a reference Pt/C material with same Pt particle size. The authors identified $Pt@TiO_x$ core-shell particles with HR-TEM for particles of 6 nm and larger, while the detailed structure of smaller particles could not be accessed due to resolution limits. As is the case here and in our previous report,[46] no CO stripping and no H_{upd} peaks could be observed with $Pt/TiO_x/C^{400°C,\ H2}$. While the tolerance to methanol was not verified in Ref. [68], it can be expected that $Pt@TiO_x$ particles would also not oxidize methanol. While the authors reported much lower ORR activity for $Pt/TiO_x/C$ than for Pt/C, comparable activities were observed for the hydrogen oxidation reaction (HOR) in acidic and alkaline medium.[68] This behavior is, again, strongly analogous to that of $Pt@FeO_x$ core-shell particles, with high HOR activity in acidic medium (Figure 4 in Ref. [69], HOR polarisation curves labelled D and E corresponding to the catalysts $Pt_{1.0}Fe_{1.0}d$

and $Pt_{2.0}Fe_{1.0}d$, respectively). The authors in Ref. [68] proposed that the strongly suppressed ORR activity but retained HOR activity for their Pt@TiO_x particles relative to Pt particles may be explained by the fact that only the Pt core is electrochemically active and O_2 (or H_2) must diffuse through the TiO_x overlayer in order to react. The electrochemical results obtained in the present study on model Fe_20_3/Pt(111) surfaces however challenge this hypothesis. First, if the Pt core had not modified the electrochemical properties of the Fe-oxide overlayer, the latter should have dissolved very quickly in acidic medium. Second, if the diffusion rate of O_2 and H_2 through the Fe-oxide layer controlled the ORR and HOR activity, respectively, the results should have shown linear increase of electrochemical activities with decreasing FeO_x overlayer thickness. However, the present study reveals an exponential increase of ORR activity with decreasing FeO_x overlayer thickness. This supports an electron tunneling effect from the Pt core through the Fe-oxide layer, the electron tunneling improving both the stability and electrochemical activity of the top surface Fe-oxide.

More theoretical and experimental work is needed however to better understand the relation between the ORR and/or HOR activity of Pt@MO_x core-shell systems and the thickness of the metal-oxide shell (e.g. Pt@FeO_x and Pt@TiO_x core-shell systems) and why the methanol oxidation reaction is suppressed altogether. Last, while the model Fe_20_3/Pt(111) surfaces reproduce well the general stability and reactivity trends of Pt@FeO_x core-shell particles in the hybrid Pt/FeNC catalysts, a notable difference exists in the lower potential limit for stability. While it is 0.45 V *vs*. RHE for the *model* surfaces, it is downshifted to at least 0.05 V *vs.* RHE for Pt@FeO_x particles in Pt/FeNC catalysts. The latter is deduced from the break-in procedure used in Ref. [46] for all RDE measurements, consisting of 20 CVs between 0.05 and 1.1 V vs. RHE. Since this break-in procedure did not remove the Fe-oxide layer (no H_{upd} signal characteristic of surface-exposed Pt was observed after the break-in), it can be concluded that the FeO_x overlayer in Pt/FeNC is stable down to this low potential. This different behaviour between *model* and real catalysts may be due to the presence of different Pt surfaces than Pt(111), or to strain effects improving the stability of FeO_x overlayer in the powder catalysts. Support for a much stronger interaction between FeO_x overlayer and Pt edge sites as well as Pt(100) surface relative to that

for Pt(111) was recently reported by Wen et al.[70] Upon formation of FeO_x by atomic layer deposition (ALD) on Pt nanoparticles, it was observed that the CO adsorption signal characteristic for CO/Pt(edge) decreased most strongly and followed closely by CO/Pt(110), while the signal for CO/Pt(111) remained intense even after several ALD cycles. This suggests preferential deposition of FeO_x on Pt edge sites and Pt(100) than on Pt(111). This in turn suggests stronger interaction between FeO_x and such Pt sites compared to Pt(111). This is in line with the stability observed down to lower potential for the powder Pt/FeNC catalyst compared to Fe_2O_3 model thin-film on Pt(111).

CONCLUSIONS

The electrochemical results on the Pt/FeNC powder catalysts with 1-2 wt % Pt identify complete tolerance to methanol while catalyzing ORR in acidic medium. DMFC polarisation curves with Pt/FeNC cathodes comprising only 40-80 μg_{Pt} cm^{-2} showed promising power performance compared to state-of-art Pt/C cathodes with 2000 μg_{Pt} cm^{-2}, allowing the utilization of high methanol concentration (5 M) at the anode without any drawback. STEM-EDXS characterization of the Pt/FeNC material with 2 wt % Pt identified the encapsulation of Pt nanoparticles by a thin Fe-oxide shell (on average, 1.3 nm), *i.e.* Pt@FeO_x core-shell structures. ^{57}Fe Mössbauer spectroscopy at low temperature identified the coexistence of Pt@FeO_x particles with FeN_x sites. In order to understand the ORR activity and stability of Pt@FeO_x particles, ultrathin films of Fe_2O_3 on Pt(111) were prepared. It was shown that the Fe-oxide layer is stable in acidic medium in the potential range 0.45 – 1.05 V vs. RHE, revealing a stabilization of the Fe-oxide by subsurface Pt(111). While Fe_2O_3 overlayers showed similar stability for different Fe_2O_3 thicknesses, the ORR activity increased exponentially with decreasing thickness. For example, the ORR activities at 0.9 V *vs*. RHE of the 1.6 and 1.0 nm Fe-oxide layers on Pt(111) were *ca* 1/70th and 1/8th that of Pt(111), respectively. Both the stability and ORR activity of Fe_2O_3 can be explained by electron-tunneling effect from Pt(111) through the ultrathin Fe-oxide shell. In addition, it is demonstrated that the deposition of even only 1 nm Fe_2O_3 on Pt(111) renders the surface fully tolerant to methanol.

From a practical viewpoint for DMFC or other direct alcohol fuel cells cathodes, the results show that Fe-oxide@Pt core particles are promising as i) methanol-tolerant, ii) stable and ORR-active particles in Pt/Fe-N-C hybrid catalysts and iii) as particles stabilizing neighboring FeN_x sites. In addition, Fe-oxide@Pt particles could be promising HOR catalyst for PEMFC anodes, with improved tolerance to many species known to poison exposed Pt nanoparticles.

ASSOCIATED CONTENT

Supporting Information. Additional STEM-EDXS characterizations of $Pt_{2.0}Fe_{1.0}d$; ^{57}Fe Mössbauer spectroscopy characterization of $Pt_{2.0}Fe_{1.0}d$; LEED pattern of 3.2-Fe_2O_3/Pt(111); O_{1s} and Fe_{2p} XPS narrow-scan spectra of 3.2-Fe_2O_3/Pt(111); CV in Ar-saturated 0.1 M $HClO_4$ of 3.2-Fe_2O_3/Pt(111); Fe_{3p}/Pt_{4f} and Fe 2p XPS spectra before and after applying CVs in different conditions; potentiodynamic EC-STM measurements of 1.6-Fe_2O_3/Pt(111); ORR activity vs. Fe_2O_3 thickness. This material is available free of charge via the Internet at http://pubs.acs.org.

AUTHOR INFORMATION

Corresponding Authors

*frederic.jaouen@umontpellier.fr, stefano.agnoli@unipd.it.

Author Contributions

The manuscript was written through contributions of all authors. All authors have given approval to the final version of the manuscript.

Funding Sources

The research leading to these results has received funding from the Fuel Cells and Hydrogen 2 Joint Undertaking under grant agreement No 779366 (CRESCENDO). This joint undertaking receives

support from the European Union's Horizon 2020 research and innovation programme, Hydrogen Europe and Hydrogen Europe Research. F.J. also acknowledges financial support from AxLR. T.K., S.A. and G.G. also acknowledge financial support from the Italian MIUR (PRIN 2015: SMARTNESS, 2015K7FZLH; PRIN2017: Multi-e, 20179337R7). G. D. acknowledges the financial support from Slovenian Research Agency (P2-0393).

ABBREVIATIONS

PEMFC, proton exchange membrane fuel cell; DMFC, direct methanol fuel cell; AEM, anion exchange membrane; ORR, oxygen reduction reaction; PGM, platinum group metal; STEM, scanning transmission electron microscopy; EDXS, energy dispersive x-ray spectroscopy; EC-STM, electrochemical scanning tunneling microscopy; CV, cyclic voltammetry; LEED, low energy electron diffraction; XPS, X-ray photoemission spectroscopy; HAADF, high-angle annular dark-field; RHE, reversible hydrogen electrode; SCE, saturated calomel electrode; BE, binding energy.

REFERENCES

(1) Katsounaros, I.; Cherevko, S.; Zeradjanin, A. R.; Mayrhofer, K. J. J. *Angewandte Chemie International Edition* **2014**, *53*, 102–121.

(2) Shao, M.; Chang, Q.; Dodelet, J.; Chenitz, R. *Chemical Reviews* **2016**, *116*, 3594−3657.

(3) Wu, Q.; Liang, J.; Yi, J.; Meng, D.; Shi, P.; Huang, Y.; Cao, R. *Dalton Trans.* **2019**, *48*, 7211–7217.

(4) Liang, Y.; Mclaughlin, D.; Csoklich, C.; Schneider, O.; Bandarenka, A. S. *Energy & Environmental Science* **2019**, *12*, 351–357.

(5) Cheng, F.; Chen, J. *Chem. Soc. Rev.* **2012**, *41*, 2172–2192.

(6) He, Q.; Cairns, E. J. *Journal of The Electrochemical Society* **2015**, *162* (14), F1504–F153922.

(7) Erikson, H.; Sarapuu, A.; Tammeveski, K. *ChemElectroChem* **2019**, *6*, 73–86.

(8) Ma, R.; Lin, G.; Zhou, Y.; Liu, Q.; Zhang, T. *npj Computational Materials* **2019**, *5*, 1–15.

(9) Wang, Y.; Chen, K. S.; Mishler, J.; Chan, S.; Cordobes, X. *Applied Energy* **2011**, *88* (4), 981–1007.

(10) Dekel, D. R. *Journal of Power Sources* **2018**, *375*, 158–169.

(11) Firouzjaie, H. A.; Mustain, W. E. *ACS Catalysis* **2020**, *10*, 225–234.

(12) Zheng, Y.; Omasta, T. J.; Peng, X.; Wang, L.; Varcoe, J. R.; Pivovar, S.; Mustain, W. E. *Energy & Environmental Science* **2019**, *12*, 2806–2819.

(13) Kamarudin, S. K.; Achmad, F.; Daud, W. R. W. *International Journal of Hydrogen Energy* **2009**, *34* (16), 6902–6916.

(14) Li, X.; Faghri, A. *Journal of Power Sources* **2013**, *226*, 223–240.

(15) Falcão, D. S.; Oliveira, V. B.; Rangel, C. M.; Pinto, A. M. F. R. *Renewable and Sustainable Energy Reviews* **2014**, *34*, 58–70.

(16) Yuan, W.; Zhou, B.; Deng, J.; Tang, Y.; Zhang, Z.; Li, Z. *International Journal of Hydrogen Energy* **2014**, *39* (12), 6689–6704.

(17) Yoshida, T.; Kojima, K. *Electrochem. Soc. Interface* **2015**, *24*, 45–49.

(18) Sui, S.; Wang, X.; Zhou, X.; Su, Y.; Riffat, S.; Liu, C.-J. *Journal of Materials Chemistry A* **2017**, *5* (5), 1808–1825.

(19) Ott, S.; Orfanidi, A.; Schmies, H.; Anke, B.; Nong, H. N.; Hübner, J.; Gernert, U.; Gliech, M.;

Lerch, M.; Strasser, P. *Nature Materials* **2020**, *19* (January), 77–86.

(20) Chattot, R.; Bacq, O. Le; Beermann, V.; Kühl, S.; Herranz, J.; Henning, S.; Kühn, L.; Asset, T.; Guétaz, L.; Renou, G.; Drnec, J.; Bordet, P.; Pasturel, A.; Eychmüller, A.; Schmidt, T. J.; Strasser, P.; Dubau, L.; Maillard, F. *Nature Materials* **2018**, *17* (September), 827–834.

(21) Li, M.; Zhao, Z.; Cheng, T.; Fortunelli, A.; Chen, C.; Yu, R.; Zhang, Q.; Gu, L.; Merinov, B. V; Lin, Z.; Zhu, E.; Yu, T.; Jia, Q.; Guo, J.; Zhang, L.; Huang, Y.; Duan, X. *Science* **2016**, *354* (6318), 1414–1419.

(22) Dhanushkodi, S. R.; Mahinpey, N.; Srinivasan, A.; Wilson, M. *Journal of Environmental Informatics* **2008**, *11* (1), 36–44.

(23) Evangelisti, S.; Tagliaferri, C.; Brett, D. J. L.; Lettieri, P. *Journal of Cleaner Production* **2017**, *142*, 4339–4355.

(24) Notter, D. A.; Kouravelou, K.; Karachalios, T.; Daletou, M. K.; Haberland, N. T. *Energy & Environmental Science* **2015**, *8*, 1969–1985.

(25) Chung, H. T.; Cullen, D. A.; Higgins, D.; Sneed, B. T.; Holby, E. F.; More, K. L.; Zelenay, P. *Science* **2017**, *357* (August), 479–484.

(26) Chen, S.; Zhang, N.; Narvaaez Villarrubia, C. W.; Huang, X.; Xie, L.; Wang, X.; Kong, X.; Xu, H.; Wu, G.; Zeng, J.; Wang, H. *Nano Energy* **2019**, *66*, 1–8.

(27) Zhang, H.; Chung, H. T.; Cullen, D. A.; Wagner, S.; Kramm, U. I.; More, K. L.; Wu, G. *Energy & Environmental Science* **2019**, *12*, 2548–2558.

(28) Jiao, L.; Li, J.; Richard, L. L.; Stracensky, T.; Liu, E.; Sun, Q.; Sougrati, M.-T.; Zhao, Z.; Yang, F.; Zhong, S.; Xu, H.; Mukerjee, S.; Huang, Y.; Myers, D. J.; Jaouen, F.; Jia, Q. *ChemRxiv* **2019**, 1–19.

(29) Ramaswamy, N.; Tylus, U.; Jia, Q.; Mukerjee, S. *Journal of the American Chemical Society* **2013**, *135*, 15443–15449.

(30) Jia, Q.; Ramaswamy, N.; Tylus, U.; Strickland, K.; Li, J.; Serov, A.; Artyushkova, K.; Atanassov, P.; Anibal, J.; Gumeci, C.; Barton, S. C.; Sougrati, M. T.; Jaouen, F.; Halevi, B.; Mukerjee, S. *Nano Energy* **2016**, *29*, 65–82.

(31) Mineva, T.; Matanovic, I.; Atanassov, P.; Sougrati, M.-T.; Stievano, L.; Clemancey, M.; Latour, J.; Jaouen, F. *ACS Catalysis* **2019**, *9*, 9359–9371.

(32) Wagner, S.; Auerbach, H.; Tait, C. E.; Martinaiou, I.; Kumar, S. C. N.; Kübel, C.; Sergeev, I.; Wille, H.-C.; Behrends, J.; Wolny, J. A.; Schünemann, V.; Kramm, U. I. *Angewandte Chemie - International Edition* **2019**, *58*, 10486–10492.

(33) Shao, Y.; Dodelet, J.; Wu, G.; Zelenay, P. *Advanced Materials* **2019**, *31*, 1–8.

(34) Martinez, U.; Babu, S. K.; Holby, E. F.; Zelenay, P. *Current Opinion in Electrochemistry* **2018**, *9*, 224–232.

(35) Piela, B.; Olson, T. S.; Atanassov, P.; Zelenay, P. *Electrochimica Acta* **2010**, *55*, 7615–7621.

(36) Sebastián, D.; Baglio, V.; Aricò, A. S.; Serov, A.; Atanassov, P. *Applied Catalysis B: Environmental* **2016**, *182*, 297–305.

(37) Martinaiou, I.; Monteverde Videla, A. H. A.; Weidler, N.; Kübler, M.; Wallace, W. D. Z.; Paul, S.; Wagner, S.; Shahraei, A.; Stark, R. W.; Specchia, S.; Kramm, U. I. *Applied Catalysis B: Environmental* **2020**, *262*, 1–13.

(38) Lo Vecchio, C.; Serov, A.; Romero, H.; Zulevi, B.; Arico, A. S.; Baglio, V. *Journal of Power* **2019**, *437*, 1–7.

(39) Santori, P. G.; Speck, F. D.; Li, J.; Zitolo, A.; Jia, Q.; Mukerjee, S.; Cherevko, S.; Jaouen, F.

Journal of The Electrochemical Society **2019**, *166* (7), F3311–F3320.

(40) Chenitz, R.; Kramm, U. I.; Lefevre, M.; Glibin, V.; Zhang, G.; Sun, S.; Dodelet, J.-P. *Energy & Environmental Science* **2018**, *11*, 365–382.

(41) Kumar, K.; Dubau, L.; Mermoux, M.; Li, J.; Zitolo, A.; Nelayah, J.; Jaouen, F.; Maillard, F. *Angewandte Chemie* **2020**, *132*, 2–11.

(42) Choi, C. H.; Baldizzone, C.; Polymeros, G.; Pizzutilo, E.; Kasian, O.; Schuppert, A. K.; Ranjbar Sahraie, N.; Sougrati, M. T.; Mayrhofer, K. J. J.; Jaouen, F. *ACS Catalysis* **2016**, *6* (5), 3136–3146.

(43) Kumar, K.; Gairola, P.; Lions, M.; Ranjbar-Sahraie, N.; Mermoux, M.; Dubau, L.; Zitolo, A.; Jaouen, F.; Mai. *ACS Catalysis* **2018**, *8*, 11264–11276.

(44) Goellner, V.; Armel, V.; Zitolo, A.; Fonda, E.; Jaouen, F. *Journal of The Electrochemical Society* **2015**, *6*, H403–H414.

(45) Choi, C. H.; Lim, H.-K.; Chung, M. W.; Chon, G.; Ranjbar-Sahraie, N.; Altin, A.; Sougrati, M.-T.; Stievano, L.; Oh, H. S.; Park, E. S.; Luo, F.; Strasser, P.; Drazic, G.; Mayrhofer, K. J. J.; Kim, H.; Jaouen, F. *Energy & Environmental Science* **2018**, *11*, 3176–3182.

(46) Mechler, A. K.; Ranjbar-Sahraie, N.; Armel, V.; Zitolo, A.; Sougrati, M.-T.; Schwammlein, J. N.; Jones, D. J.; Jaouen, F. *Journal of The Electrochemical Society* **2018**, *165* (13), 1084–1091.

(47) Shaikhutdinov, S. K.; Weiss, W. *Surface Science Letters* **1999**, *432*, L627–L634.

(48) Genuzio, F.; Sala, A.; Schmidt, T.; Menzel, D.; Freund, H. *J. Phys. Chem. C* **2014**, *118*, 29068−29076.

(49) Fadley, C. S. *Progress in Surface Science* **1984**, *16* (3), 275–388.

(50) Wilms, M.; Kruft, M.; Bermes, G.; Wandelt, K. *Review of Scientific Instruments* **1999**, *70* (9), 3641.

(51) Sebastian, D.; Serov, A.; Artyushkova, K.; Atanassov, P.; Arico, A. S.; Baglio, V. *Journal of Power* **2016**, *319*, 235–246.

(52) Liu, S.; Wu, J.; Pan, C.; Hwang, B. *Journal of Power Sources* **2014**, *250*, 279–285.

(53) Léger, J. M. *Journal of Applied Electrochemistry* **2001**, *31*, 767–771.

(54) Gloaguen, F.; Léger, J. M.; Lamy, C. *Journal of Applied Electrochemistry* **1997**, *27*, 1052–1060.

(55) Sougrati, M. T.; Goellner, V.; Schuppert, A. K.; Stievano, L.; Jaouen, F. *Catalysis Today* **2016**, *262*, 110–120.

(56) Teng, X.; Black, D.; Watkins, N. J.; Gao, Y.; Yang, H. *Nano Letters* **2003**, *3* (2), 261–264.

(57) Sun, Y.; Qin, Z.; Lewandowski, M.; Carrasco, E.; Sterrer, M.; Shaikhutdinov, S.; Freund, H. *Journal of Catalysis* **2009**, *266* (2), 359–368.

(58) Figuerola, A.; Fiore, A.; Corato, R. Di; Falqui, A.; Giannini, C.; Micotti, E.; Lascialfari, A.; Corti, M.; Cingolani, R.; Pellegrino, T.; Cozzoli, P. D.; Manna, L. *Journal of the American Chemical Society* **2008**, No. 11, 1477–1487.

(59) Hong, H.; Hu, L.; Li, M.; Zheng, J.; Sun, X.; Lu, X.; Cao, X.; Lu, J.; Gu, H. *Chemistry - A European Journal* **2011**, *17*, 8726–8730.

(60) Kuhlenbeck, H.; Shaikhutdinov, S.; Freund, H. *Chemical Reviews* **2013**, *113*, 3986–4034.

(61) Biesinger, M. C.; Payne, B. P.; Grosvenor, A. P.; Lau, L. W. M.; Gerson, A. R.; Smart, R. S. C. *Applied Surface Science* **2011**, *257* (7), 2717–2730.

(62) Zeng, Z.; Chang, K.; Kubal, J.; Markovic, N. M. *Nature Energy* **2017**, *17070* (May), 1–9.

(63) Neufeld, O.; Toroker, M. C. **2015**, 24129–24137.

(64) Mahmoud, A.; Deleuze, P.-M.; Dupont, C. *J. Chem. Phys.* **2018**, *148*, 204701–204709.

(65) Kosmala, T.; Calvillo, L.; Agnoli, S.; Granozzi, G. *ACS Catalysis* **2018**, *8* (3).

(66) Shin, D.; Sinthika, S.; Choi, M.; Thapa, R.; Park, N. *ACS Catalysis* **2014**, *4* (11), 4074–4080.

(67) Pacchioni, G.; Freund, H. *Chemical Reviews* **2013**, *113* (6), 4035–4072.

(68) Stühmeier, B. M.; Selve, S.; Patel, M. U. M.; Geppert, T. N.; Gasteiger, H. A.; El-Sayed, H. A. *ACS Appl. Energy Mater.* **2019**, *2*, 5534–5539.

(69) Schuppert, A.; Jaouen, F.; Jones, D. WO/2017/042520. WO/2017/042520, 2020.

(70) Wen, Y.; Cai, J.; Zhang, J.; Yang, J.; Shi, L.; Cao, K.; Chen, R.; Shan, B. *Chem. Mater.* **2019**, *2* (100), 101–111.

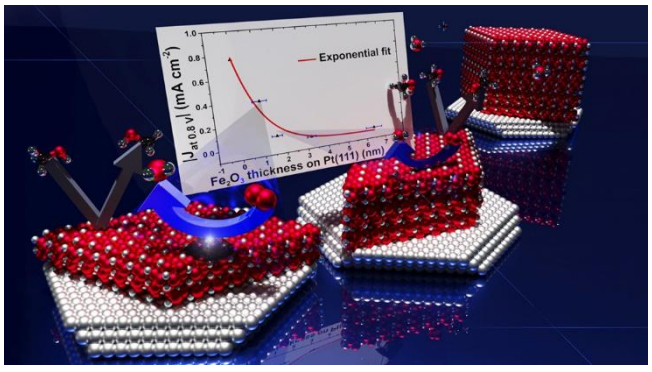

TOC